Journal of Power Sources 196 (2011) 4396–4403

Contents lists available at ScienceDirect

Journal of Power Sources

journal homepage: www.elsevier.com/locate/jpowsour

Electrochemical characterisation of solid oxide cell electrodes for hydrogen production

Carlos Bernuy-Lopez*, Ruth Knibbe, Zeming He, Xiaojian Mao, Anne Hauch, Karsten A. Nielsen

Fuel Cells and Solid State Chemistry Division, Risø National Laboratory for Sustainable Energy, Technical University of Denmark, 4000 Roskilde, Denmark

ARTICLE INFO

Article history:
Received 30 July 2010
Received in revised form 26 October 2010
Accepted 29 October 2010
Available online 9 November 2010

Keywords:
Solid oxide cells
Impedance spectroscopy
Lanthanum strontium manganite
Yttria stabilised zirconia
Strontium titanate

ABSTRACT

Oxygen electrodes and steam electrodes are designed and tested to develop improved solid oxide electrolysis cells for H_2 production with the cell support on the oxygen electrode. The electrode performance is evaluated by impedance spectroscopy testing of symmetric cells at open circuit voltage (OCV) in a one-atmosphere set-up. For the oxygen electrode, nano-structured $La_{0.75}Sr_{0.25}MnO_3$ (LSM25) is impregnated into a LSM25/yttria stabilised zirconia (YSZ) composite, whereas for the steam electrode, nano-structured Ni and $Ce_{0.8}Gd_{0.2}O_{2-\delta}$ (CGO) is impregnated into a $Sr_{0.94}Ti_{0.9}Nb_{0.10}O_{3-\delta}$ (STN) backbone. In the present study, the best performing oxygen electrode is a LSM25-YSZ composite with 20% porosity and impregnated with a LSM25 solution measuring a polarisation resistance (R_p) of 0.12 Ω cm^2 at 850 °C in oxygen. For the steam electrode, the best performance is obtained for a STN backbone, sintered at 1200 °C and impregnated with CGO/Ni, with an R_p of 0.08 Ω cm^2 at 850 °C in 3% H_2O/H_2.

1. Introduction

Solid oxide cells (SOCs) are high temperature electrochemical devices which can be operated as a fuel cell to convert fuel to electricity; or an electrolysis cell to convert electricity into fuel. More specifically, a solid oxide electrolysis cell (SOEC) can convert excess electricity plus H_2O and/or CO_2 to hydrogen or synthesis gas (H_2 + CO).

SOEC testing has been reported already since the 1980s [1,2]. This work started with testing yttria stabilised zirconia (YSZ) electrolyte supported systems with a Ni/YSZ steam electrode and a lanthanum strontium manganite (LSM)/YSZ oxygen electrode. More recently this SOEC interest has been revived with focus on the development of improved cell performance [3,4]. To date, the majority of the SOEC testing has been based on steam electrode supported cells with a Ni/tetragonal YSZ (t-YSZ) support; Ni/YSZ steam electrode; thin YSZ electrolyte and LSM/YSZ oxygen electrode. However, testing and durability studies of SOECs with significantly different compositions have also been reported [5–9].

At the Risø DTU high initial electrolysis performance [10,11] has been obtained for steam electrode supported solid oxide electrolysis cells (SOECs) having an LSM/YSZ composite oxygen electrode. The LSM/YSZ oxygen electrode microstructure can endure 1500 h of electrolysis testing at −0.5 A cm^{-2} [12,13] but shows irreversible degradation under higher current density [14].

A problem presented with the steam electrode supported cell is that gas diffusion limitations can be introduced at high current densities [15,16]. To avoid such limitations it was postulated by Ni et al. to fabricate an oxygen electrode supported cell, i.e. producing an SOC optimised for SOEC purposes [15].

Several groups have produced oxygen electrode supported SOCs for SOFC application with varying success (Table 1) [17–20]. The cells have typically been built around a zirconia electrolyte and an LSM/YSZ oxygen electrode support, except one cell was fabricated using a $Pr_{0.35}Nd_{0.35}Sr_{0.3}MnO_{3-x}$ (PNSM)/$Sm_{0.2}Ce_{0.8}O_{1.95}$ (SDC) composite as an oxygen electrode support with a thin, SDC/YSZ electrolyte [18]. As a variation sintering temperatures and production techniques were used for the electrolyte production, not all cells are gas tight. Assuming the oxygen and steam electrode are sealed, the electrolyte gas tightness can be evaluated by comparing the theoretical cell voltage and the measured voltage at open circuit voltage (OCV) (Table 1). The most gas tight electrolyte was fabricated by Yamahara et al. [20] who used a sintering temperature of 1250 °C.

The area specific resistance (ASR) values are also presented in Table 1, however it should be noted that the ASR values are not all directly comparable. In general, it is suggested that the cells fabricated by Yamahara et al. [20], Chen et al. [19] and Liu et al. [18] have the highest performance, however the different cell size will effect the conversion resistance. Although it is difficult to conclude which cell performs the best without further detailed analysis, the serial resistances (R_s) can be directly compared.

* Corresponding author at: Fuel Cells and Solid State Chemistry Division, Risø DTU, National Laboratory for Sustainable Energy, Technical University of Denmark, 4000 Roskilde, Denmark. Tel.: +45 46775617; fax: +45 46775858.
E-mail address: belo@risoe.dtu.dk (C. Bernuy-Lopez).

0378-7753/$ – see front matter © 2010 Elsevier B.V. All rights reserved.
doi:10.1016/j.jpowsour.2010.10.102

Table 1
Production parameters and cell characteristics of various LSM/t-YSZ support cells reported in literature [17–20].

Oxygen electrode[a]	Electrolyte (μm)	Steam electrode	T_s (°C)[b]	OCV (V)[c]	ASR (Ω cm^2)[d]	R_s (Ω cm^2)	Ref.
LSM95 SSZ	SSZ (26)	Pt	1250	1.08 1.14	0.90	0.25	Zhao et al. [17]
PNSM SSC	SSC (11) YSZ (4)	Ni SSC	1300	0.99 1.1	0.52	0.13	Liu et al. [18]
LSM YSZ	YSZ (27)	LSCM CGO	1200	1.08 1.1	0.58	0.12	Chen et al. [19]
LSM SYSZ	SYSZ (~13)	Ni SYSZ	1250	~1.1 1.1	0.64	0.19	Yamahara et al. [20]

[a] $(La_{0.8}Sr_{0.2})_{0.95}MnO_3$ (LSM95); $Sc_{0.1}Ce_{0.01}Zr_{0.89}O_{2-x}$ (SSZ); $Pr_{0.35}Nd_{0.35}Sr_{0.3}MnO_{3-x}$ (PNSM); $Sm_{0.2}Ce_{0.8}O_{1.95}$ (SSC); $Gd_{0.2}Ce_{0.8}O_{1.9}$ (CGO); $La_{0.75}Sr_{0.25}Cr_{0.5}Mn_{0.5}O_3$ (LSCM); $Sc_{0.1}Y_{0.01}Zr_{0.89}O_{2-x}$ (SYSZ).
[b] T_s – sintering temperature.
[c] Open circuit voltage (OCV) including measured and theoretical at 800 °C, with 3% H_2O/H_2 supplied to the steam electrode and air supplied to oxygen electrode (except Zhao et al. which has oxygen supplied to the oxygen electrode).
[d] Area specific resistance (ASR) measured at OCV in aforementioned conditions (except Yamarhara et al. which is reported at maximum power).

The highest R_s is obtained in the cell fabricated by Zhao et al. [17], which could be attributed to reaction between the LSM95 phase and the electrolyte. Similarly, although Yamahara et al. [20] have used a very thin electrolyte, the R_s is relatively high 0.19 Ω cm^2. In comparison, although the electrolyte in the cell produced by Chen et al. [19] is as thick as the cell fabricated by Zhao et al. [17], the lower sintering temperature (1200 vs. 1250 °C) appears to have avoided oxygen electrode/electrolyte reaction yielding the lowest R_s of 0.12 Ω cm^2.

For an oxygen electrode supported SOC, the oxygen electrode support/electrolyte half cell is sintered prior to steam electrode deposition and sintering [17–20]. As such a sintering temperature range limitation is introduced. The lower limit is presented by the temperature required to densify the electrolyte (~1210 °C for YSZ) and the upper limit is presented by the point at which the oxygen electrode and electrolyte react (~1250 °C for LSM/YSZ) [21]. From the LSM/YSZ oxygen electrode perspective these temperatures are relatively high in comparison to similar LSM/YSZ oxygen electrode sintering temperatures for steam electrode supported cells (ca. <1100 °C). As such, the larger anticipated grain size would reduce the three phase boundary length, decreasing the oxygen electrode performance [22]. However, from an electrolyte and support perspective the sintering temperatures required for the oxygen electrode supported cell are relatively low in comparison to the sintering temperatures typically used in the steam electrode supported cell (ca. 1300 °C). With reduction in sintering temperature the sintering of the YSZ electrolyte and the t-YSZ in the support are reduced – potentially affecting the cell gas tightness and strength respectively. In addition the support porosity must be optimised. Higher support porosity allows for easy electrode impregnation, however, the volume fraction of LSM and t-YSZ is consequently reduced which may compromise electronic connectivity and mechanical strength respectively.

The more traditional steam electrode – Ni/YSZ also presents issues for electrolysis operation as the Ni/YSZ steam electrode degrades during redox cycling. Furthermore, operation under high steam concentration can cause strong Ni agglomeration. A recent study [23] on $Sr_{0.94}Ti_{0.9}Nb_{0.10}O_{3-\delta}$ (STN) impregnated with nano-sized nickel and $Ce_{0.8}Gd_{0.2}O_{2-\delta}$ (CGO) showed promising performance for obtaining a stable and high-performing steam electrode. STN is an A-site deficient $SrTiO_3$ perovskite where the Ti^{4+} B-site is doped with Nb^{5+} which acts as an extrinsic dopant – increasing the STN electronic conductivity. STN is A-site deficient to avoid SrO secondary phase formation. STN has negligible electrochemical activity therefore must be impregnated with active particles to improve the electrochemical response. This activity can also be improved by introducing oxygen vacancies in the STN backbone structure through reduction – improving the ionic and electronic conductivity.

From a production perspective, the steam electrode sintering temperature is an important parameter to investigate as increasing STN grain size would consequently decrease potential TPB sites. Furthermore, STN may interact with the adjacent YSZ electrolyte by Sr or Ti reactivity/dissolution [24,25] forming deleterious interfacial phases which could negatively impact the electrode performance.

The focus of this study is to understand the effect of the processing parameter limitations of oxygen electrode supported cells on electrochemical performance of LSM/YSZ and STN. For the support and oxygen electrode the porosity, sintering temperature and impregnation are investigated. For the STN steam electrode the sintering temperature, reduction temperature, electrode thickness and impregnation are investigated. To avoid confusion the cell components will be discussed using the following terminology – the LSM/t-YSZ support will be referred to as the 'support'; LSM/YSZ oxygen electrode as the 'oxygen electrode' and the STN steam electrode as 'steam electrode'.

2. Experimental

To gauge the effect of the processing parameters on the cell performance, symmetric cells were fabricated and electrochemically tested. For the oxygen electrode symmetric cells, oxygen electrode supported cells were fabricated with a thick LSM/t-YSZ support, thin LSM/YSZ oxygen electrode and a thin YSZ electrolyte (Fig. 1(a)). For the steam electrode, electrolyte supported symmetric cells were produced with thin steam electrodes and a thick YSZ electrolyte (Fig. 1(b)). These symmetric cell configurations were chosen as they are considered similar to the electrodes that would be used in a full cell configuration.

2.1. Oxygen electrode

Three different oxygen electrodes (OE1, OE2 and OE3) were fabricated and tested. The electrodes were tested in the form of a symmetrical cell encompassing five distinct layers: a 15 μm thick Sc-doped yttrium stabilised zirconia (Sc-YSZ, 10 mol% Sc_2O_3, 3.1 mol% Y_2O_3 and 0.25 wt% Al_2O_3 doped ZrO_2) electrolyte sandwiched by two 30 μm thick $La_{0.75}Sr_{0.25}MnO_3$ and 8 mol% Y_2O_3 doped ZrO_2 composite (LSM/YSZ) oxygen electrode layers and two 300 μm thick $La_{0.75}Sr_{0.25}MnO_3$ and 3 mol% Y_2O_3 doped ZrO_2 composite (LSM/t-YSZ) support layers (Fig. 1(a)). The symmetric cells were fully tape cast and sintered in air at 1210 °C for the OE1 samples and at 1260 °C for the OE2 and OE3 samples. Apart from the sintering temperature, the cells differ in pore-former quantity added during fabrication in order to obtain support porosity of 20, 30 and 35% for OE1, OE2 and OE3 samples respectively.

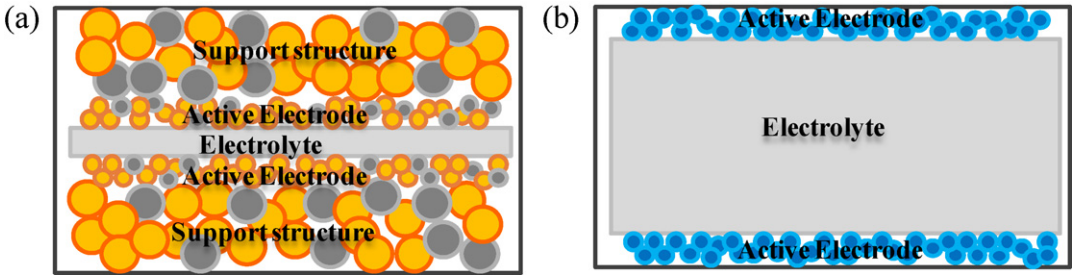

Fig. 1. Schematic of the symmetric cell configuration for the (a) oxygen electrode and (b) steam electrode cells.

These non-impregnated samples are considered reference samples (labelled R). A set of these samples were impregnated under vacuum with a mixed salt solution giving a $La_{0.75}Sr_{0.25}MnO_3$ (LSM25) composition after calcination at 600 °C for 1 h (labelled I). Hence, OE1, OE2 and OE3 have been electrochemically tested with and without LSM25 impregnation.

After production, the cell phase purity, microstructure, in-plane conductivity, porosity and electrochemical performance were characterised. The in-plane electrical conductivity of the support was measured at room temperature using the Van der Pauw technique [26], where a Model 580 micro-ohmmeter (Keithley, UK) was used to measure the 4-terminal resistance. The porosity and the pore size were measured by a Micromeritics mercury porosimeter. The phase purity was determined using X-ray diffraction (XRD) employing a Stoe diffractometer with Cu Kα radiation.

The cell microstructure was investigated using a Zeiss Crossbeam scanning electron microscope (SEM) equipped with a field emission gun (FEG). For SEM, the cells were prepared by vacuum embedding cell pieces in epoxy (Struers EpoFix) followed by grinding and polishing. The samples were inspected in low voltage (LVSEM) mode, using an InLens detector, operating the FEG at 1 keV with uncoated samples [27]. LVSEM micrographs highlight the LSM grain interconnectivity in the electrode and support structures. Fractured, uncoated, LSM25 impregnated samples were inspected operating the Zeiss Crossbeam at 15 keV using the InLens detector.

2.2. Steam electrode

For characterising the steam electrode, electrolyte supported symmetrical cells were fabricated. The supporting electrolyte is a 200 μm thick dense 8 mol% Y_2O_3 doped ZrO_2 (YSZ) electrolyte and is sandwiched by two $Sr_{0.94}Ti_{0.9}Nb_{0.10}O_{3-\delta}$ (STN) electrode backbones (Fig. 1(b)). The STN powder was deposited by spray coating. Two electrode thicknesses were prepared: 20 μm and 30 μm, labelled as STN_A and STN_B respectively. The spray-coated cells were sintered in air for 3 h at two different temperatures: 1200 °C (labelled L) and 1250 °C (labelled H). These non-impregnated and unreduced samples are considered reference samples (labelled R). A set of the symmetric cells were reduced in 9% H_2/N_2 for 17 h at 1100 °C (labelled Red). To enhance the electrode catalytic properties, $Ce_{0.8}Gd_{0.2}O_{2-\delta}$ (CGO) and 10 wt% Ni mixed solution was impregnated into the STN backbone and subsequently calcined at 350 °C in air for 3 h (labelled CGONi). The impregnation procedure is described elsewhere [28]. The impregnation and subsequent calcinations were repeated three times.

After production, the cell microstructure was investigated using SEM. The SEM samples were prepared in the same manner as the oxygen electrode supported symmetric cells and were subsequently carbon coated. The steam electrode symmetric cells were observed using the aforementioned Zeiss Crossbeam operated at 12 keV, in backscattered electron mode.

2.3. Impedance spectroscopy

The symmetric cells were characterised by means of electrochemical impedance spectroscopy (EIS) in a one-atmosphere rig. For current collection, Pt-paste was applied onto the electrode surfaces. Typically, at least two of the same samples were placed in the rig and measured simultaneously in order to ensure reproducibility. Impedance analysis of the symmetric cells was performed at open circuit voltage using a Solatron 1260 Frequency Analyser. The impedance spectra were recorded from 82 540 Hz to 0.08 Hz with 6 points per frequency decade.

The oxygen electrode symmetric cell impedance data were collected at temperatures between 600 and 850 °C, at 50 °C intervals during both heating and cooling, in air and pure O_2 atmospheres. The steam electrode symmetric cell impedance data were collected at temperature between 650 and 850 °C at 50 °C intervals during heating and 100 °C intervals during cooling with 3% H_2O in pure hydrogen.

3. Results

3.1. Oxygen electrode

The in-plane conductivity of OE1, OE2 and OE3 are presented in Table 2. The room temperature in-plane conductivity is the highest for OE1 (1.5 S cm^{-1}) and the lowest for OE3 (0.1 S cm^{-1}). Although the measured values are proportionally less than what is anticipated from dense room temperature LSM electrical conductivity measurements (ca. 30 S cm^{-1} [29]), the LSM electronic conductivity is reported to be dependent on sintering temperature and microstructure [30].

LVSEM micrographs of OE1 and OE3 are presented in Fig. 2. A micrograph of OE2 has not been included as it is similar to the microstructure of OE3. The benefit of the LVSEM technique is that it highlights the LSM electron conducting phase – which appears bright in the micrograph. Non-conducting LSM, YSZ and the epoxy filled pores all appear dark when using this operating mode. It can be clearly observed that the LSM in the support and the oxygen electrode is both electronically conducting and interconnected.

Between the three cells the major differences are the sintering temperature, the pore size distribution and support porosity. The support structure in all cases consists of LSM and t-YSZ. The OE1 support microstructure is relatively similar to the oxygen electrode

Table 2
In-plane electronic conductivity and secondary phases for the tested LSM/t-YSZ symmetric cells. The volume fraction of LSM:YSZ is 48:52 for the support and the oxygen electrode for all the three sets of samples.

	OE1	OE2	OE3
In-plane conductivity (S cm^{-1})	1.5	0.5	0.1
XRD – secondary phases	mZrO_2	$La_2Zr_2O_7$	$La_2Zr_2O_7$

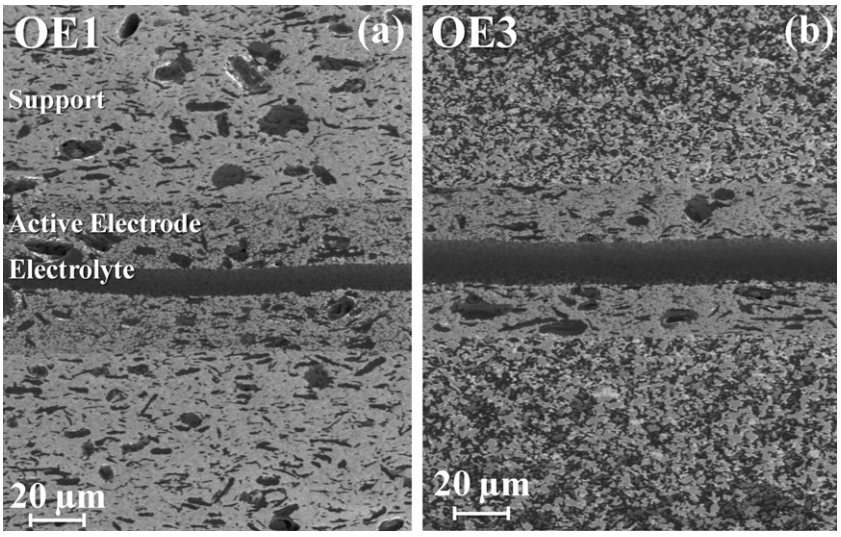

Fig. 2. InLens SEM pictures for (a) OE1 and (b) OE3.

microstructure whereas the OE2 and OE3 support microstructures are markedly different to the oxygen electrode microstructure.

Table 3 is a collation of the oxygen electrode supported symmetric cells R_p values at 850 °C in pure oxygen and air. OE3 has the highest R_p (0.79 Ω cm^2 at 850 °C in oxygen), which is approximately halved to 0.38 Ω cm^2 for the OE2 sample. The best performance is from the OE1 with an R_p of 0.26 Ω cm^2 under the same operating conditions.

Fig. 3 shows the Bode-type plots for the reference samples (OE1_R, OE2_R and OE3_R) of the three samples at 850 °C in pure O_2 (Fig. 3(a)) and for OE2 at 650 °C, 750 °C and 850 °C in pure O_2 (Fig. 3(b)). In order to increase the frequency resolution dZ'/d ln (Hz) is plotted vs. frequency in all the Bode-type plots shown. OE2 and OE3 are dominated by a low frequency arc about 10 Hz. The OE1 cell is also dominated by a low frequency arc, where the characteristic frequency is ~5 Hz. This low frequency arc in all cells is thermally activated (Fig. 3(b)).

Impregnating the oxygen electrode with nano-sized LSM25 improves the cell performance in all cases (Table 3). However, this improvement is not equal for all samples and atmospheres. The OE3 cells show an R_p improvement by a factor of 2.2–4.4 (calculated as the worse scenario and best scenario taking into account the error values) when operated in pure O_2 and 850 °C (0.25 vs. 0.79 Ω cm^2). At the same operating conditions, OE2 impregnation improves the R_p by 1.4–1.6 times (0.25 vs. 0.38 Ω cm^2) and OE1 impregnation improves the R_p by 1.1–2.7 times (0.12 vs. 0.26 Ω cm^2). Although the observation that OE3 improves the most after impregnation could suggest that the more open support structure allows for improved impregnation, the OE2 samples, which have higher support porosity than OE1, show the weakest improvement after infiltration. Despite the impregnation having a relatively weak effect on OE1, it still maintains the best performance with an R_p of 0.12 Ω cm^2 at 850 °C in oxygen.

Fig. 4 is a micrograph across the support/oxygen electrode interface of OE3 – relatively dense oxygen electrode on top section and support on lower section. Small patches of infiltrate are located at the support/oxygen electrode interface. Here it is observed that the infiltrate can easily penetrate through the porous support, but the high density of the oxygen electrode severely impedes impregnation into the oxygen electrode.

Table 3
Serial resistances for OE1, OE2 and OE3. Polarisation resistances for both references and impregnated samples for OE1, OE2 and OE3 in air and pure O_2 at 850 °C.

	OE1	OE2	OE3
R_s	0.09 ± 0.06	2.39 ± 0.12	1.81 ± 0.30
R_p			
O_2			
Reference	0.26 ± 0.01	0.38 ± 0.01	0.79 ± 0.14
Impregnated	0.16 ± 0.06	0.25 ± 0.01	0.25 ± 0.04
Air			
Reference	0.44 ± 0.04	0.49 ± 0.04	0.85 ± 0.24
Impregnated	0.24 ± 0.07	0.30	0.40 ± 0.04

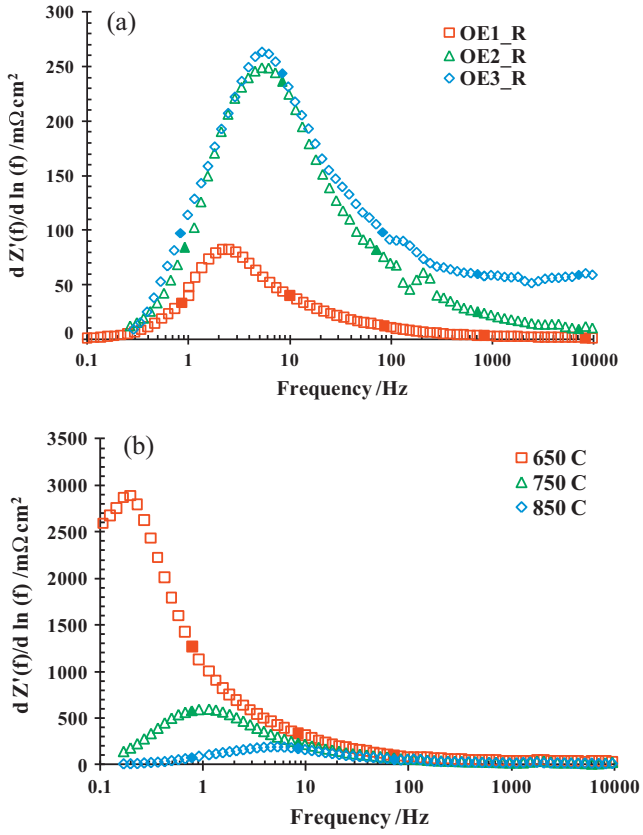

Fig. 3. Bode-type plot (dZ'/d ln (Hz) vs. frequency) calculated from the impedance data recorded for (a) OE1, OE2 and OE3 reference samples in pure O_2 at 850 °C and (b) OE2 at 650 °C, 750 °C and 850 °C. Filled and large symbols are selected frequencies at 82 kHz, 8.2 kHz, 825 Hz, 82 Hz, 8.2 Hz, and 0.82 Hz.

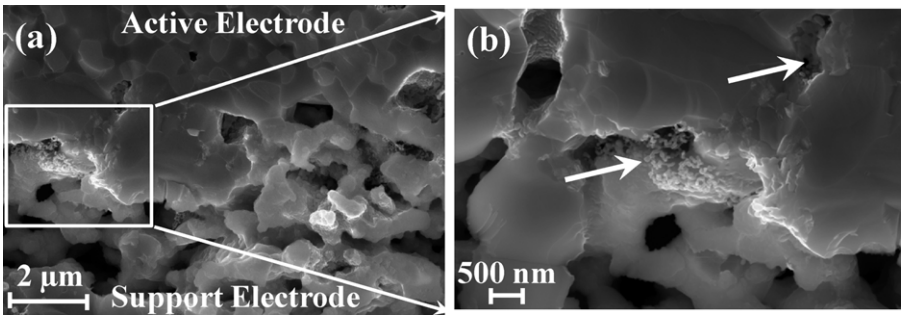

Fig. 4. SEM micrographs across the support/oxygen electrode interface showing the LSM infiltrate. (b) A magnified view of interface area indicated in (a), highlighting the location of the LSM infiltrate (marked by arrows).

The serial resistance, R_s, for the cells at 850 °C is presented in Table 3. There is a notable R_s difference between the three sets of samples. OE2 and OE3 have comparable R_s values (2.39 and 1.81 Ω cm^2 respectively) while OE1 shows much lower R_s values (0.09 Ω cm^2). From XRD $La_2Zr_2O_7$ is detected in both OE2 and OE3 samples (Table 2). However, from SEM-EDS analysis it was not possible to locate the $La_2Zr_2O_7$ as a separate phase either at the electrolyte/oxygen electrode interface or at the LSM/YSZ grain interfaces. The $La_2Zr_2O_7$ phases may be difficult to detect due to the reaction grain size which may be significantly smaller than the interaction volume size of the probing electron beam.

3.2. Steam electrode

Fig. 5(a) and (b) is SEM micrographs of STN_A_L_R. The electrolyte is dense and free of major defects. The STN electrode has an even grain size (<1 μm) with a homogenously distributed porosity. The electrode is well bonded on the electrolyte and does not show major signs of elemental diffusion across the electrode/electrolyte interface. Fig. 5(c) is a higher magnification SEM image of the STN_A_L_R after Ni/CGO impregnation. The higher average atomic number of the Ni makes the infiltrate bright in the backscattered micrograph. The open microstructure of the STN backbone allows for easy impregnation.

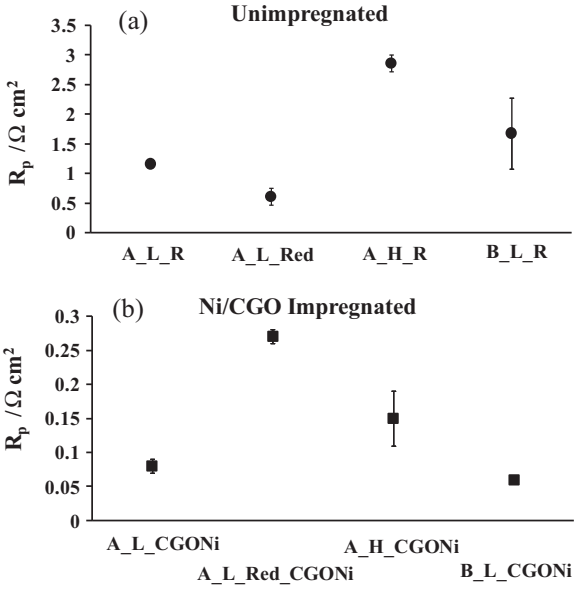

Fig. 6. Polarisation resistances obtained from impedance measurements for both (a) references and (b) impregnated samples in 3% H_2O/H_2 at 850 °C.

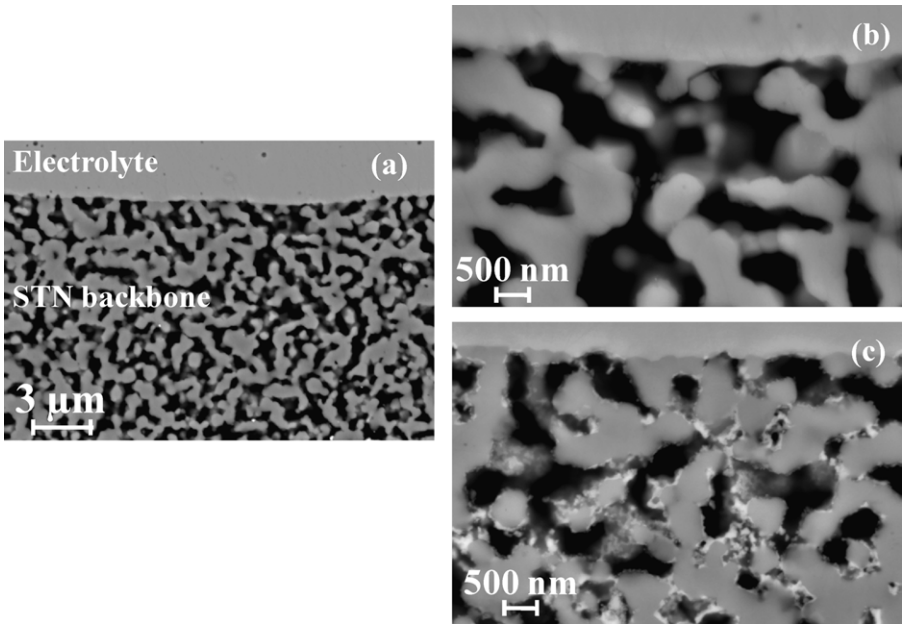

Fig. 5. SEM micrographs of STN_A_L before impregnation at (a) low magnification, (b) higher magnification and (c) after Ni/CGO infiltration.

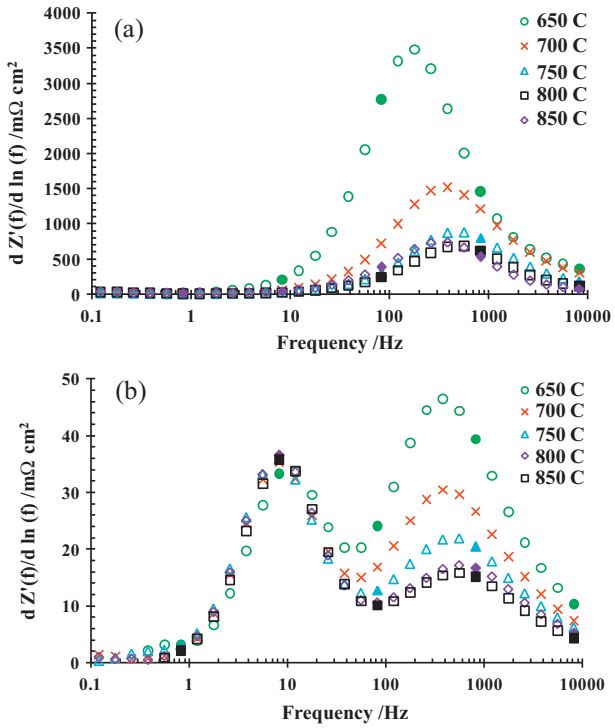

Fig. 7. Bode-type plot ($dZ'/d\ln(Hz)$ vs. frequency) calculated from the impedance data recorded for (a) STN_A_L reference samples and (b) STN_A_L_CGONi impregnated samples in 3% H_2O/H_2 at 650, 700, 750, 800, 850 °C. Large symbols are selected frequencies at 8.2 kHz, 825 Hz, 82 Hz, 8.2 Hz, and 0.82 Hz.

Fig. 6(a) shows the R_p values obtained from the EIS measurements for the unimpregnated reference samples STN_A_L_R, STN_A_L_Red, STN_A_H_R and STN_B_L_R. By impregnating the samples the R_p values reduce by an order of magnitude (Fig. 6(b)).

For the unimpregnated samples (Fig. 6(a)) the thin, low temperature sintered, reduced sample shows the best performance and the thin, high sintering temperature sample shows the worst performance. This trend does not hold after impregnation, the cell that was found to perform the best prior to impregnation performs the worst after impregnation (STN_A_L_Red). However, some consistent observations are made, namely there is little difference between using a thin (20 μm) or thick (30 μm) STN backbone and the lower sintering temperature of 1210 °C is consistently better performing than the higher sintering temperature of 1250 °C. The low sintered, non-reduced, CGO/Ni impregnated samples (STN_A_L_CGONi and STN_B_L_CGONi) show the best performance. STN_A_L_R has an R_p of 1.16 Ω cm² at 850 °C and 3% H_2O/H_2 which after CGO/Ni impregnation improves by a factor of 15, to 0.08 Ω cm² at the same conditions.

Fig. 7 shows the Bode-type plots calculated from the impedance data for both reference (Fig. 7(a)) and impregnated (Fig. 7(b)) samples as function of temperature with 3% H_2O/H_2 held constant. For the reference sample one thermally activated process can be seen, which has a characteristic frequency of ~300 Hz at 850 °C and ~100 Hz at 650 °C. For the impregnated samples two processes can be seen: one at low and one at high frequency. The low frequency process has a characteristic frequency of 8 Hz and is not thermally activated. This process is therefore assigned to a gas diffusion process. The high frequency process has a characteristic frequency of ~300 Hz at 850 °C and is thermally activated. This process is therefore related to the electrochemical processes. The characteristic frequency of the high frequency process is very similar in the impregnated and unimpregnated samples – although the resistance is an order of magnitude larger in the latter.

4. Discussion

4.1. Oxygen electrode

Three measurements can shed light on the effect of the processing parameters on the cell performance – in-plane conductivity measurements, R_p and R_s. The in-plane conductivity measurements describe the LSM grain connectivity in the support structure. The R_s provides a more complicated piece of information as it contains information on the electrolyte oxide ion conductivity, the LSM electronic conductivity through support and the oxygen electrode and finally the contact resistance between the LSM and the YSZ electrolyte. The R_p provides information on the oxygen electrode. The major microstructural parameters known to affect the R_p are the YSZ connectivity, LSM connectivity and three phase boundary (TPB) length of the oxygen electrode per volume [22]. The TPB is the boundary where the three phases meet – the YSZ ionic conductor, LSM electronic conductor and pore for gas supply/removal. The R_p information is further complicated if the in-plane conductivity is too low.

The in-plane conductivity is reduced by increasing the support structure porosity – as anticipated. As the in-plane conductivity collectively describes the LSM–LSM connectivity it should not be heavily affected by reactions at the LSM/YSZ interfaces which are found to form in the high sintering temperature samples.

However, LSM/YSZ reaction is noticeable in the R_s. $La_2Zr_2O_7$ formation at the LSM/YSZ interfaces dramatically increases the contact resistance between the electronic conducting LSM in the electrode and the oxide ion conducting, YSZ electrolyte. Although the in-plane conductivity may also affect the R_s, the decrease in the in-plane conductivity is not proportional to the decrease in the R_s. Rather, the OE2 and OE3 both show an R_s increase which is more than one order of magnitude larger than OE1's R_s. As such the R_s increase is attributed to the $La_2Zr_2O_7$ formation at the oxygen electrode/electrolyte interface.

Although the values in Table 1 are for 800 °C, it is clear that the R_s of OE2 and OE3 (Table 3) is significantly worse than the reported values in oxygen electrode supported cells in literature [17–19]. However, the OE1 R_s is comparable to the R_s measured by Chen et al. [19].

The thermal activation of the R_p (Fig. 3(b)) indicates that the processes observed here are related to electrochemical process. The R_p is the highest for the OE2 or OE3 cells. This could be attributed to a combination of factors: higher sintering temperature which affects the oxygen electrode by changing the LSM structure, the porosity and/or forming resistive $La_2Zr_2O_7$ at the LSM/YSZ interfaces. Both the OE2 and OE3 samples are sintered at a high temperature and as such have a changed oxygen electrode density and also have $La_2Zr_2O_7$ formation at the LSM/YSZ interfaces. An increased, oxygen electrode density would decrease the TPB concentration. The formation of resistive $La_2Zr_2O_7$ at the LSM/YSZ interfaces will either eliminate this position as a TPB (effectively decreasing the TPB) or increase the TPB resistance – ultimately increasing the R_p. From this work it is not possible to conclude whether it is the change in electrode density or the $La_2Zr_2O_7$ formation which is dominating the R_p increase. However, it is clear that the $La_2Zr_2O_7$ formation has a less dramatic effect on the R_p than on the R_s.

The aim of impregnation is to extend the TPB length in the oxygen electrode. Although increased support porosity of OE2 and OE3 is detrimental to the in-plane conductivity, the higher support porosity should be beneficial for impregnation. However, the impregnation effect is strongest for the OE3 cell (largest support structure porosity) and weakest for the OE2 cell (2nd largest support structure porosity). This suggests that although the high support structure porosity allows for easy LSM25 impregnation through the support, the oxygen electrode remains relatively dense

and the LSM25 impregnation through the oxygen electrodes can be expected to be similar. This is also confirmed from SEM imaging of the various oxygen electrodes where only minor amounts of LSM25 infiltrate are found in the oxygen electrode region (Fig. 4). Even though the LSM25 infiltrate does not easily impregnate into the oxygen electrode, by merely decorating the oxygen electrode top surface and the large pores in the oxygen electrode, the TPB length is increased to reduce the R_p. Impregnation may be very sensitive to minor variations in support and electrode structure therefore it is difficult to conclude precisely why OE1 improves more than OE2 after impregnation even though the support porosity is lower.

Despite OE1 having the lowest support porosity, the support porosity is still sufficient to allow for LSM impregnation through the support structure to the oxygen electrode. This is advantageous from a strength perspective as the reduced porosity allows for an increased LSM and t-YSZ connectivity potentially allowing higher electronic conductivity and mechanical strength.

Jørgensen et al. reported on the performance of several electrolyte supported LSM/YSZ symmetric cells as a function of different production parameters [22,31]. The best cell reported in these studies had an R_p of 0.12 Ω cm^2 at 850 °C in air, when sintered between 950 and 1000 °C. In the same manner, Kim et al. reported an R_p of 0.14 Ω cm^2 at the same conditions for a cell of the nominally similar characteristics [32]. In the present work an R_p of 0.24 Ω cm^2 was measured in OE1_I at 850 °C in air – which is a factor of two larger than the reported values for the oxygen electrode on electrolyte supported cells. Such difference is attributed to the sintering temperature and reduction of the TPB length per volume [31].

4.2. Steam electrode

As the STN backbone has negligible catalytic activity compared to the nano-sized, Ni/CGO particles in all cases the R_p decreased by an order of magnitude after Ni/CGO impregnation [18].

Increasing STN sintering temperature increases the backbone R_p. Although not presented, the R_s values were not strongly affected by the sintering temperature. The negative effect of increased sintering temperature is still observed after Ni/CGO impregnation – as such it is attributed to the increased grain size associated with higher sintering temperatures.

Pre-reduction of the cell did not affect the R_s, but decreased the R_p. However, after Ni/CGO impregnation the improvement that is observed from the reduced STN backbone is lost and the reduced backbone structure exhibits the worst impregnated performance. From literature [23,28] it is known that reducing STN increases the Ti^{3+}concentration in the STN however as the cation diffusion is sluggish in STN the increased Ti^{3+}concentration may be isolated to the particle surface. Therefore the poor performance of the Ni/CGO impregnated reduced backbone structure may be related to the change in the STN surface defect structure which affects the nano particle nucleation and growth.

In general the nature of the Ni/CGO impregnation may be sensitive to various STN backbone parameters including – STN surface area, pore structure and STN defect surface structure. This work is beyond the scope of this paper, but will be addressed in the future.

Previously, CGO has been impregnated into a STN backbone yielding an R_p of 0.12 Ω cm^2 at 850 °C in 3% H_2O/H_2. From Fig. 6, it can be seen that a slightly better result was obtained with Ni/CGO impregnation (R_p of 0.08 Ω cm^2 for STN_A_L_CGONi and 0.06 Ω cm^2 for STN_B_L_CGONi at 850 °C in 3% H_2O/H_2). Furthermore, these impregnated STN electrodes perform better than the commonly used Ni-YSZ steam electrode, which have been reported to have an R_p of up to 0.11 Ω cm^2 at the same operating conditions [33]. The impregnated STN shows improved performance in comparison to Ni-YSZ due to the nano-sized Ni and CGO inclusions which increase the TPB close to the electrolyte. Furthermore, CGO at these temperatures and oxygen partial pressures exhibits mixed electronic and ionic conductivity which can further enhance the electrochemical performance.

4.3. Cell overview

In order to estimate the performance of a full electrolysis cell, made from the best of the developed electrodes, following values can be used:

- Ni/CGO impregnated low temperature sintered STN steam electrode – R_p = 0.08 Ω cm^2 (850 °C, 3% H_2O/H_2).
- LSM/t-YSZ support sintered at 1210 °C, impregnated with LSM25 – R_p = 0.24 Ω cm^2 (850 °C, air).
- Low temperature sintered, thin (15 μm) electrolyte 1210 °C – R_s = 0.09 Ω cm^2 (850 °C).

For a full cell this would yield an ASR of 0.41 Ω cm^2. Although this does not include the gas conversion resistance, the ASR is competitive with other oxygen electrode supported cells (Table 1).

5. Conclusions

5.1. Oxygen electrode

- Oxygen electrode supported symmetric cells were producing with the best performance achieved for the sample sintered at 1210 °C, showing no $La_2Zr_2O_7$ formation. At higher sintering temperatures, 1260 °C, resistive $La_2Zr_2O_7$ formed, which increased R_s and R_p.
- The high sintering temperature decreases the TPB length producing cells with R_p values higher than conventional LSM/YSZ electrodes.
- Electrode backbone (LSM/YSZ) needs to be more open in order for the impregnated LSM to access the vicinity of the electrolyte, hence decreases the R_p
- Impregnation of the electrode, forming nano-sized LSM25 decreases the R_p. The impregnation was facilitated, though not consistently, by a sufficiently open and porous LSM/t-YSZ support microstructure.

5.2. Steam electrode

- Increased STN backbone sintering temperature adversely affects the R_p.
- STN backbone pre-reduction did not improve the R_s, rather it also reduced the R_p and the beneficial electrode impregnation effect.
- The highest performance is obtained with the STN_L_CGONi sample sintered at 1200 °C, unreduced and impregnated.

Acknowledgments

Areva SA (France) is acknowledged by the authors for financial support as well as the Risø DTU funded “SOE Celler” Project.

References

[1] W. Donitz, G. Dietrich, E. Erdle, R. Streicher, Int. J. Hydrogen Energy 13 (1988) 283–287.
[2] W. Donitz, R. Streicher, Chem. Ing. Tech. 52 (1980) 436–438.
[3] W. Zhang, B. Yu, J. Chen, J. Xu, Prog. Chem. 20 (2008) 778–787.
[4] A Brisse, J. Schefold, M. Zahid, Int. J. Hydrogen Energy 33 (2008) 5375–5382.
[5] W.S. Wang, Y.Y. Huang, S.W. Jung, J.M. Vohs, R.J. Gorte, J. Electrochem. Soc. 153 (2006) A2066–A2070.
[6] V.I. Sharma, B. Yildiz, J. Electrochem. Soc. 157 (2010) B441–B448.
[7] K. Eguchi, T. Hatagishi, H. Arai, Solid State Ionics 1245 (1996) 86–88.
[8] A. Momma, T. Kato, Y. Kaga, S. Nagata, J. Ceram. Soc. Jpn. 105 (1997) 369–373.

[9] J. Hartvigsen, S. Elangovan, J.E. O'Brien, C. Stoots, J. Herring, Electrochem. Soc. Trans. 7 (2007) 357–363.
[10] S.H. Jensen, P.H. Larsen, M. Mogensen, Int. J. Hydrogen Energy 32 (2007) 3253–3257.
[11] A. Hauch, S.H. Jensen, M. Mogensen, S. Ramousse, J. Electrochem. Soc. 153 (2006) A1741–A1747.
[12] A. Hauch, S.D. Ebbesen, S.H. Jensen, M. Mogensen, J. Mater. Chem. 18 (2008) 2331–2340.
[13] A. Hauch, S.D. Ebbesen, S.H. Jensen, M. Mogensen, J. Electrochem. Soc. 155 (2008) B1184–B1193.
[14] R. Knibbe, M.L. Traulsen, A. Hauch, S.D. Ebbesen, M. Mogensen, J. Electrochem. Soc. 157 (2010) B1209–B1217.
[15] M. Ni, M.K.H. Leung, D.Y.C. Leung, J. Power Sources 163 (2006) 460–466.
[16] R. Knibbe, S.D. Ebbesen, M. Mogensen, Electrochem. Soc. Trans. 28 (2010) 77–87.
[17] C. Zhao, R. Liu, S. Wang, T. Wen, Electrochem. Commun. 11 (2009) 842–845.
[18] M. Liu, D. Dong, F. Zhao, J. Gao, D. Dong, X. Liu, G. Meng, J. Power Sources 182 (2008) 585–588.
[19] X.J. Chen, Q.L. Liu, S.H. Chan, N.P. Brandon, K.A. Khor, Electrochem. Commun. 9 (2007) 767–772.
[20] K. Yamahara, C.P. Jacobson, S.J. Visco, L.C. De Jonghe, Solid State Ionics 176 (2005) 451–456.
[21] J.A.M. Van Roosmalen, E.H.P. Cordfunke, Solid State Ionics 52 (1992) 303–312.
[22] M.J. Jørgensen, S. Primdahl, C. Bagger, M. Mogensen, Solid State Ionics 139 (2001) 1–11.
[23] P. Blennow, K.K. Hansen, L.R. Wallenberg, M. Mogensen, Electrochem. Soc. Trans. 13 (2008) 181–194.
[24] K. Kleveland, M.A. Einarsrud, C.R. Schmidt, S. Shamsili, S. Faaland, K. Wiik, T. Grande, J. Am. Ceram. Soc. 82 (1999) 729–734.
[25] N.Q. Minh, J. Am. Ceram. Soc. 76 (1993) 563–588.
[26] L.J. van der Pauw, Philips Tech. Res. Rep. 1 (1958) 13.
[27] K. Thyden, Y.L. Liu, J.B. Bilde-Sorensen, Solid State Ionics 178 (2008) 1984–1989.
[28] P. Blennow, K.K. Hansen, L.R. Wallenberg, M. Mogensen, Solid State Ionics 180 (2009) 63–70.
[29] J. Mizusaki, Y. Yonemura, H. Kamata, K. Ohyama, N. Mori, H. Takai, H. Tagawa, M. Dokiya, K. Naraya, T. Sasamoto, H. Inaba, T. Hashimoto, Solid State Ionics 132 (2000) 167–180.
[30] S.P. Jiang, J. Mater. Sci. 43 (2008) 6799–6833.
[31] M.J. Jørgensen, M. Mogensen, J. Electrochem. Soc. 148 (2001) A433–A442.
[32] J.D. Kim, G.D. Kim, J.W. Moon, Y.I. Park, W.H. Lee, K. Kobayashi, M. Nagai, C.E. Kim, Solid State Ionics 143 (2001) 379–389.
[33] S. Primdahl, M. Mogensen, Solid State Ionics 152–153 (2002) 597–608.